

# Selective coherent x-ray diffractive imaging of displacement fields in (Ga,Mn)As/GaAs periodical wires

A. A. Minkevich,<sup>1,\*</sup> E. Fohtung,<sup>1</sup> T. Slobodskyy,<sup>1</sup> M. Riotte,<sup>1</sup> D. Grigoriev,<sup>1</sup>  
M. Schmidbauer,<sup>2</sup> A. C. Irvine,<sup>3</sup> V. Novák,<sup>4</sup> V. Holý,<sup>5</sup> and T. Baumbach<sup>1</sup>

<sup>1</sup>*Institute for Synchrotron radiation, Forschungszentrum Karlsruhe, 76344 Eggenstein-Leopoldshafen, Germany*

<sup>2</sup>*Leibniz-Institut für Kristallzüchtung, Max-Born-Straße 2, D-12489 Berlin, Germany*

<sup>3</sup>*Microelectronics Research Centre, Cavendish Laboratory,  
University of Cambridge, Cambridge CB3 0HE, United Kingdom*

<sup>4</sup>*Institute of Physics of the ASCR, Cukrovarnicka 10, 162 00 Praha, Czech Republic*

<sup>5</sup>*Department of Condensed Matter Physics, Faculty of Mathematics and Physics,  
Charles University, Ke Karlovu 5, 121 16 Praha, Czech Republic*

(Dated: November 17, 2018)

Coherent x-ray diffractive imaging is extended to high resolution strain analysis in crystalline nanostructured devices. The application potential is demonstrated by determining the strain distribution in (Ga,Mn)As/GaAs nanowires. By separating diffraction signals in reciprocal spaces, individual parts of the device could be reconstructed independently by our inversion procedure. We demonstrate the method to be effective for material specific reconstruction of strain distribution in highly integrated devices.

PACS numbers: 61.05.cp, 62.20.-x, 42.30.Rx, 75.50.Pp

Nanoscope elastic strain analysis is crucial for understanding physical properties and fabrication processes of crystalline nanostructures and devices. In epitaxial nanostructures, strain distribution is strongly correlated to their shape and composition. It is also an important driving force for self-assembling processes [1].

In conventional x-ray diffraction experiments information about shape, composition and strain is obtained *indirectly* by quantitative comparison of measured and simulated reciprocal-space distributions of scattered intensity [2]. Simulations are based on a model with preliminary assumptions about detailed shape, composition and strain profile, which will be confirmed by the experimental results as long as the model structure fits to the reality.

A *direct* determination of the density of the scattering centers from the reciprocal-space distribution of the scattered intensity is however not possible, unless a special *phase-retrieval method* is used. This phase-retrieval procedure known as coherent x-ray diffractive imaging (CXDI) has a potential to become a powerful technique for the structural characterization of small objects and micro-sized semiconductor devices [3, 4, 5, 6, 7, 8, 9, 10]. The method principle is based on the iterative loop of direct and inverse Fourier transformation (FT) (towards the experimental intensity distribution and back to the sample space) and it may refine the genuine object density distribution  $\tilde{\rho}(\mathbf{r})$  even by starting from a model which is far from reality [11, 12].

In case of crystalline nano-objects the distribution of the scattered amplitude in reciprocal space around a reciprocal lattice point (RLP) is given by

$$E(\mathbf{Q}) \sim \int d^3\mathbf{r} \varrho_{\mathbf{h}}(\mathbf{r}) e^{-i\mathbf{h}\cdot\mathbf{u}(\mathbf{r})} e^{-i(\mathbf{Q}-\mathbf{h})\cdot\mathbf{r}}. \quad (1)$$

Here,  $\mathbf{h}$  and  $\mathbf{Q}$  denote the reciprocal-lattice vector and the position vector in reciprocal space (scattering vector), respectively,  $\varrho_{\mathbf{h}}(\mathbf{r})$  is the corresponding Fourier component of electron density and  $\mathbf{u}(\mathbf{r})$  is the displacement field with respect to the non-strained lattice.

Once the phase of the scattered radiation is known, direct space amplitude  $\varrho_{\mathbf{h}}(\mathbf{r})$  and phase  $\mathbf{h}\cdot\mathbf{u}(\mathbf{r})$  can be obtained by inverse FT, within the validity of the kinematical scattering theory (first Born approximation).

An important step in the phase-retrieval loop is the application of the direct(real)-space constraints (see [11], among others). Usually, the direct-space constraint has the form of an *a-priori* known support function determining the region in direct space, where the complex electron density  $\tilde{\rho}(\mathbf{r}) = \varrho_{\mathbf{h}}(\mathbf{r}) \exp(-i\mathbf{h}\cdot\mathbf{u}(\mathbf{r}))$  may differ from zero. The first demonstration of the possibility of strain imaging by phase retrieval using support constraint on particular example of weakly strained Pb nanocrystal was recently illustrated in [7]. Later it has been shown, however, that the knowledge of the support constraint alone is not generally sufficient for the phase retrieval of diffraction pattern from highly strained crystals [13], but the problem may be overcome by introducing additional constraints. Such a suitable constraint in direct space is the use of a-priori knowledge to limit the allowed values of strain in the iterative process [6, 13].

The diffraction amplitudes of compositional layered nanoobjects can be understood as an interference sum of individual wave field contributions scattered from the different material regions. We may define firstly a non-perturbed state of the nanoobject by assuming for each material region idealized homogeneous composition and strain, spatially limited by the shapes of the individual nanostructures. Secondly we define the perturbation by

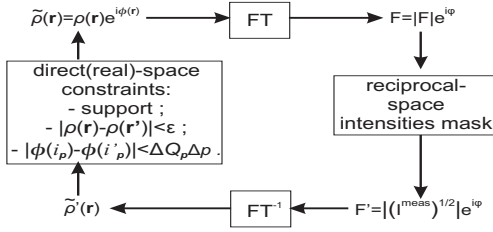


FIG. 1: Schematic diagram of the iterative loop of our phase retrieval algorithm.  $\mathbf{r}$  and  $\mathbf{r}'$  in "direct(real)-space constraints" box correspond to the neighbouring points within one constituent crystal and  $\epsilon$  defines the threshold of electron density uniformity.  $i_p$  and  $i'_p$  are the neighbouring points along  $p$ -direction (normally lateral or vertical) and  $\Delta p$  corresponds to the step along this direction (achieved resolution).

taking now the effects of non-uniform strain relaxation and possible compositional fluctuations within previously homogeneous layer region of the crystals into account. Then, *each* wave field contribution is the result of convolution of two FTs: One is the individual reciprocal shape function which leads to intensity decreases at least with  $q^{-2}$  with respect to the unperturbed RLP of that material. The other one corresponds to the FT of  $\tilde{q}(\mathbf{r})$  containing the spatial fluctuations in amplitude (compositional fluctuation) and phase (displacement field). The spread of the later FT in frequency space is dependent on the maximum gradient values of displacements in the layers and related to the strain-induced broadening of diffracted signal  $\Delta Q$  around RLP ( $\Delta Q_p$  - along particular  $p$  direction). That fact allows to transform the "limited frequency constraint" into the direct space constraint of limited component of the displacement gradient. Therefore, in addition to the standard support constraint we implement complementary direct-space constraints, namely, the uniformity of electron density (amplitudes) for each constituent crystal component and the requirement of continuity of the displacement variations (of phase) (see Fig. 1).

Now, let us consider the constraint for the vertical frequencies. In elastically strained-layer nano-objects the layer regions of different composition have considerably different *averaged* vertical lattice parameters. The resulting mean vertical lattice misfit between these regions leads to the separation of their diffraction maximums in  $q_z$ -direction (see Fig. 3) and to a shift between their whole individual contributions in reciprocal space by  $\Delta h$ .

Mostly  $\Delta h$  is sufficiently large compared to the maximum gradient of displacement field *within* the individual layers. If it is also sufficiently large compared to the main contribution of the reciprocal shape functions, reciprocal space regions are distinguishable, where the major influence of scattered intensity stems mainly from one individual material type. That consequently permits to reconstruct  $\tilde{q}$  for the individual constituent parts of the nanoobject separately.

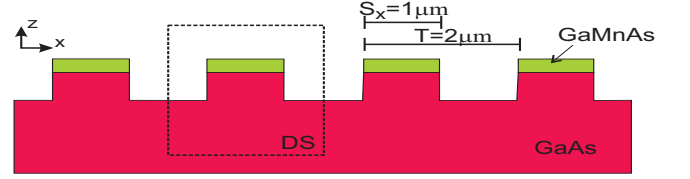


FIG. 2: (Color online) Schematic cross-section of the GaMnAs/GaAs periodical wires perpendicular to their direction (in the plane of the diffraction experiment). The direct space (DS) area attained by the periodical object diffracted signal sampling in RS is marked by the dashed line region.

Experimentally, CXDI can be applied to individual nanoobjects like wires and dots, if sufficient high photon flux density is available. In order to gain in the radiation flux density, microfocusing optics could be used [14]. Another way to overcome the problem is the use of periodical objects. If the scattering coherent volume contains a large number of equally spaced identical objects, we gain constructive interference concentrating and amplifying diffracted intensity into so-called grating rods [2]. These rods are separated by  $\Delta q_x = 2\pi/T$ , where  $T$  is a period size. The maximum intensity of the scattered radiation in rods is given by  $I_{\text{exp}} = I_1 \frac{N}{N_c} N_c^2 = I_1 N N_c$  where  $N$  is the number of the periods irradiated by the primary wave,  $N_c$  is the number of coherently irradiated periods, and  $I_1$  is the maximum intensity scattered from a single wire. Therefore, if we use an ideally coherent primary wave, the scattered intensity is substantially enhanced, since it is proportional to  $N^2$ . Consequently sampling in reciprocal space can be performed in a wider range, where measured intensities are without coherent magnification already negligibly small.

Strain analysis in III-V semiconductor nanostructures composed of GaAs and (Ga,Mn)As is performed to demonstrate the potential of CXDI for investigation of application-relevant nanoobjects. Diluted magnetic semiconductors, of which (Ga,Mn)As is a prominent example, have acquired great attention for tunability of their magnetic properties and thus for their potential in spintronic applications [15, 16]. It has been shown that, e.g., their magnetocrystalline anisotropy can be substantially affected by elastic strain [17]. One way to induce controlled spatial variation of the strain is lithographic patterning of the GaMnAs layer after the epitaxial growth. Due to the positive lattice mismatch between (Ga,Mn)As and GaAs, depending mainly on the concentration of Mn interstitial atoms [18], epitaxial (Ga,Mn)As layers deposited on GaAs substrates are biaxially compressed. After creation of a periodic sequence of thin wires and groves (surface grating), the film can relax freely at the edges of the wires.

In the investigated structures the period of wires is  $T = 2 \mu\text{m}$  and the nominal wire width is  $S_x = 1 \mu\text{m}$ . A 200 nm thick (Ga,Mn)As layer with a nominal Mn

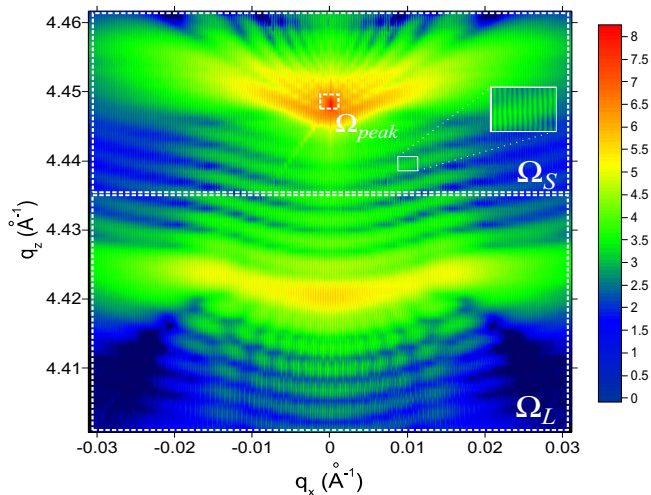


FIG. 3: (Color online) Measured reciprocal space map (log 10 of intensities) from (Ga,Mn)As/GaAs periodical wires.  $\Omega_S$  and  $\Omega_L$  confine the diffuse scattering regions from GaAs and (Ga,Mn)As respectively.

concentration of about 7% was grown onto a (001)GaAs substrate. The periodic wire structure was prepared by electron-beam lithography and reactive ion etching with an etching depth of approx. 700 nm (see Fig. 2). The (Ga,Mn)As surface wires were oriented along the  $[1\bar{1}0]$  direction. The technological details can be found elsewhere [17].

The wires do not contain large structure defects like dislocations, stacking faults, or precipitates that would give rise to considerable x-ray diffuse scattering. X-ray diffuse scattering from point-like defects such as  $\text{As}_{\text{Ga}}$  antisites, Mn substitutional and interstitial atoms [18] lies far below the detection limit of the experimental setup. Therefore, from the view-point of the experimental method used, the wires represent an ideal crystal structure with a two-dimensional distribution of the elastic displacement vector  $\mathbf{u}(x, z)$  in the plane  $xz$  perpendicular to the wire direction.

Diffraction measurements were performed at ID10B beamline at the ESRF. The x-rays from an in-vacuum undulator source were monochromatized by a diamond(111) crystal to  $E = 8$  keV. The cross-section of the primary beam was  $0.2 \times 0.2$  mm<sup>2</sup>. High resolution reciprocal-space images (RSI) were measured by use of a Si(111) crystal analyzer. The result in vicinity of the 004 RLP is shown in Fig. 3. The RSI  $q_x q_z$  plane is perpendicular to the alignment of the wires.

Two well separated features in the 004 RSI correspond to the major influence areas of the 004 reciprocal lattice points of GaAs and (Ga,Mn)As respectively (the corresponding difference in Bragg angles is about 0.2 degree). Grating maxima exhibiting a horizontal spacing of about  $\sim 3 \times 10^{-4} \text{ \AA}^{-1}$  can be clearly resolved proving the in-plane coherence length of the incoming x-ray beam to be much

larger than the  $2 \mu\text{m}$  wire period (see the magnified inset in Fig. 3). Since the lower sampling limit of RSM envelope corresponds to the rod periodicity, the oversampling ratio of the measured signal in  $q_x$  direction is defined as  $\sigma_x = \frac{T}{S_x}$ . In our case the wire width  $S_x$  occupies the half of the grating period  $T$  and consequently the oversampling rate is about  $\sigma_x = 2$  in  $q_x$  direction. The internal symmetry of the wire in lateral direction decreases the unknown information twice.

The dynamical diffraction peak of the semi-infinite GaAs substrate cannot be taken into account since this region violates the presumption of the phase retrieval method. The eliminated experimental data near the GaAs reciprocal lattice point (marked by  $\Omega_{peak}$  in Fig. 3) allowed to vary freely during reconstruction process [19].

The support in direct space is chosen on the basis of growth parameters and is finalized using Parseval theorem being applied separately to the scattering regions  $\Omega_L$  and  $\Omega_S$  in RSI shown in Fig. 3. Performing the phase-retrieval algorithm the Fourier components of electron densities  $\rho_h(\mathbf{r})$  of (Ga,Mn)As and GaAs are assumed to be not affected by elastic deformation and shall vary only with composition.

From the diffraction pattern one can conclude on a large vertical misfit between the (Ga,Mn)As and GaAs regions, allowing us to divide the measured RSI in two regions  $\Omega_L$  and  $\Omega_S$  (see Fig. 3). Each of them serves further for independent reconstruction of phase and amplitudes in the corresponding composite parts (Ga,Mn)As and GaAs of the wire, respectively. The results are depicted in Fig. 4. The reproducibility of the obtained solutions was proven performing a series of inversion cycles starting from different sets of random phases of the scattered radiation. The error metric is defined as  $E_k^2 = \frac{\sum_{i=1}^N (|F_i^{calc}| - \sqrt{I_i^{meas}})^2}{\sum_{i=1}^N I_i^{meas}}$ , where  $|F_i^{calc}|$  is the magnitude of the calculated amplitude and  $I_i^{meas}$  is the measured intensity of point  $i$  in the RSI. The error metric is found to be on the level of  $10^{-3}$  for the (Ga,Mn)As part and becomes even smaller, around  $10^{-6}$ , when inverting the GaAs part. The direct-space resolution achieved is about  $10 \times 10$  nm<sup>2</sup>.

From the results of the independent phase reconstructions of the (Ga,Mn)As and GaAs volumes of the wires the following observations can be made:

- (i) During the reconstruction of the GaAs part the average amplitude in the free-standing wire appears to be close to that one in the (Ga,Mn)As (see Fig. 4). This is in good agreement with the fact that the amplitudes of structure factors of GaAs and (Ga,Mn)As unit cells containing 7% Mn differ by less than 1 percent.
- (ii) The variation of the reconstructed phase fields (i.e., the fields of the relative vertical displacement component Fig. 5(a)) behave continuous at the boundary between the (Ga,Mn)As and GaAs volumes. That fact further supports the validity of our reconstruction process.
- (iii) Finally, the combination of both independent re-



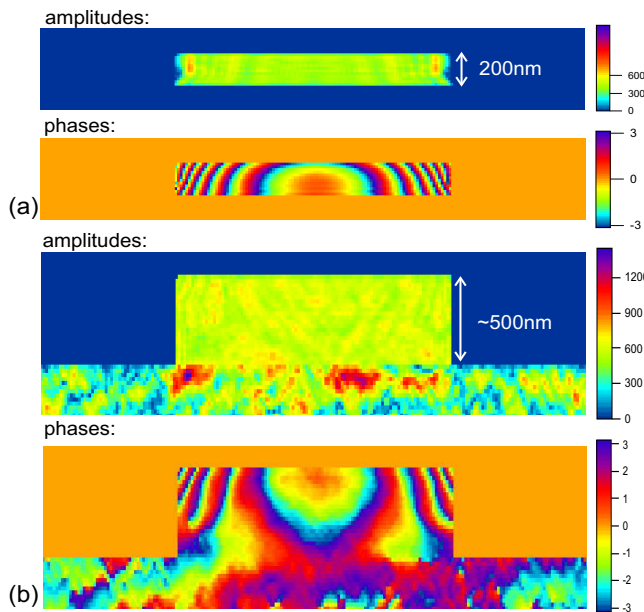


FIG. 4: (Color online) Results of reconstructions (a) of  $\Omega_L$  area of the RSI (see Fig. 3) corresponding to the (Ga,Mn)As part, (b) of  $\Omega_S$  area corresponding to the GaAs part. For the dimensions of direct space of periodic objects see Fig. 2.

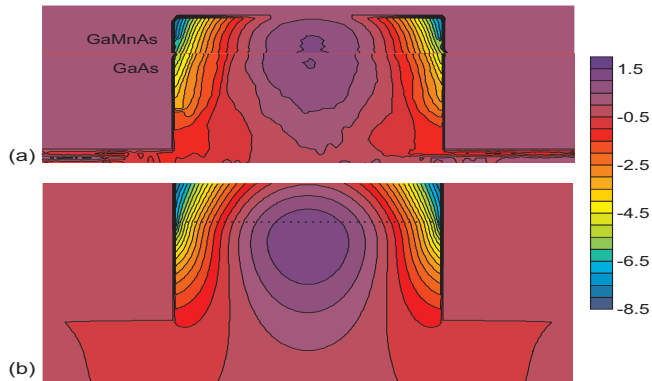


FIG. 5: (Color online) Contour maps of the vertical component  $u_z$  of the displacement vector in the (Ga,Mn)As/GaAs wire relative to the wire state before the relaxation (in Å) (a) directly reconstructed (calculated from the two phases maps shown in Fig. 4), (b) obtained numerically by finite-element simulations.

constructions into one leads after taking the FT to the same RSI as in the Fig. 3 down to the error of  $3 \times 10^{-2}$ . This shows that even overlapping regions in RSI can be independently reconstructed, when the difference in intensity levels between the intensity maxima and the edge of the cut map is at least 2 orders of magnitudes.

We do not interpret the non-homogeneous amplitudes in the GaAs substrate part (under the wire). For this region strain variation and compositional variation are certainly very small. Therefore the missing signal data in the RSI close to the strong dynamical peak (excluded

from the diffraction pattern to be reconstructed) is an essential loss of information and leads to expected instabilities in the reconstructed amplitudes in Fig. 4(b).

Numerical finite-element method (FEM) calculations were performed to simulate the strain field inside the (Ga,Mn)As/GaAs wires. Simulation used the experimentally verified value of 0.35% for the lattice mismatch between the GaAs substrate and the (Ga,Mn)As layer containing 7% Mn. The Poisson ratio and the Young modulus of GaAs were used as an approximation for (Ga,Mn)As. The results of the simulations are shown in Fig. 5(b). The excellent agreement between simulated (FEM) and reconstructed strain field distributions proves the high quality of the reconstruction process.

In summary, we illustrated the ability of CXDI based on our phase-retrieval algorithm to study non-uniform strain relaxation in strained layer nanoobjects and for the first time succeeded to reconstruct the related displacement fields. Reproducible convergence of the CXDI method has been obtained even for strongly inhomogeneously strained objects. The reconstruction procedure takes benefit from the material-specific nature of CXDI arising from compositionally driven lattice misfit. That enables individual analysis of the corresponding compositional constituents of the structure. The continuous field of displacement can be also recovered by building up the strained inhomogeneous system as a whole. The quantitative values of displacement field reconstruction have been validated using the elasticity theory. Sub ten nanometer resolution of the displacement field in direct space was achieved. The availability of a robust direct reconstruction method will allow to gain precise knowledge about multicompositional strained nanoobjects.

The work has been supported by the NAMASTE project funded by the European Union.

Authors thank to A. Singh and O. Konovalov for preparing the experimental setup.

\* andrey.minkevich@iss.fzk.de

- [1] O. Schmidt, *Lateral Alignment of Epitaxial Quantum dots* (Springer, New York, 2007).
- [2] V. Holy, U. Pietsch, and T. Baumbach, *High resolution X-Ray scattering from Thin Films and Multilayers* (Springer Verlag, 1999).
- [3] I. Robinson and R. Harder, *Nature Materials* **8**, 291 (2009).
- [4] J. Miao, et al., *Nature* **400**, 342 (1999).
- [5] H. N. Chapman, et al., *J. Opt. Soc. Am. A* **23**, 1179 (2006).
- [6] A. A. Minkevich, et al., *Phys. Rev. B* **76**, 104106 (2007).
- [7] M. A. Pfeifer, et al., *Nature* **442**, 63 (2006).
- [8] S. Marchesini, et al., *Phys. Rev. B* **68**, 140101(R) (2003).
- [9] G. J. Williams, et al., *Phys. Rev. Lett.* **97**, 025506 (2006).
- [10] P. Thibault, et al., *Science* **321**, 379 (2008).
- [11] J. R. Fienup, *Appl. Opt.* **21**, 2758 (1982).

- [12] V. Elser, *J. Opt. Soc. Am. A* **20**, 40 (2003).
- [13] A. A. Minkevich, T. Baumbach, M. Gailhanou, and O. Thomas, *Phys. Rev. B* **78**, 174110 (2008).
- [14] C. G. Schroer, et al., *Phys. Rev. Lett.* **101**, 090801 (2008).
- [15] I. Žutić, J. Fabian, and S. D. Sarma, *Rev. Mod. Phys.* **76**, 323 (2004).
- [16] T. Jungwirth, et al., *Rev. Mod. Phys.* **78**, 809 (2006).
- [17] J. Wunderlich, et al., *Phys. Rev. B* **76**, 054424 (2007).
- [18] J. Mašek, J. Kudrnovský, and F. Máca, *Phys. Rev. B* **67**, 153203 (2003).
- [19] Y. Nishino, J. Miao, and T. Ishikawa, *Phys. Rev. B* **68**, 220101(R) (2003).